Earth and Planetary Science Letters 404 (2014) 144–153

Contents lists available at ScienceDirect

Earth and Planetary Science Letters

www.elsevier.com/locate/epsl

Migration of a coarse fluvial sediment pulse detected by hysteresis in bedload generated seismic waves

D.L. Roth [a,*], N.J. Finnegan [a], E.E. Brodsky [a], K.L. Cook [b], C.P. Stark [c], H.W. Wang [d]

[a] Department of Earth and Planetary Sciences, University of California, Santa Cruz, USA
[b] GFZ German Research Centre for Geosciences, Helmholtz Centre Potsdam, Germany
[c] Lamont–Doherty Earth Observatory, Columbia University, Palisades, USA
[d] Department of Hydraulic & Ocean Engineering, National Cheng Kung University, Tainan, Taiwan

ARTICLE INFO

Article history:
Received 29 January 2014
Received in revised form 14 July 2014
Accepted 15 July 2014
Available online 21 August 2014
Editor: P. Shearer

Keywords:
dam removal
hysteresis
sediment pulse
sediment transport
fluvial geomorphology
fluvial seismology

ABSTRACT

Seismic signals near rivers are partially composed of the elastic waves generated by bedload particles impacting the river bed. In this study, we explore the relationship between this seismic signal and river bedload transport by analyzing high-frequency broadband seismic data from multiple stations along the Chijiawan River in northern Taiwan following the removal of a 13 m check dam. This dam removal provides a natural experiment in which rapid and predictable changes in the river's profile occur, which in turn enables independent constraints on spatial and temporal variation in bedload sediment transport. We compare floods of similar magnitudes with and without bedload transport, and find that the amplitude of seismic shaking produced at a given river stage changes over the course of a single storm when bedload transport is active. Hysteresis in the relationship between bedload transport and river stage is a well-documented phenomenon with multiple known causes. Consequently, previous studies have suggested that hysteresis observed in the seismic amplitude-stage response is the signature of bedload transport. Field evidence and stream profile evolution in this study corroborate that interpretation. We develop a metric (Ψ) for the normalized magnitude of seismic hysteresis during individual floods. This metric appears to scale qualitatively with total bedload transport at each seismic station, indicating a dominance of transport on the rising limbs of both storms. We speculate that hysteresis at this site arises from time-dependent evolution of the bed, for example due to grain packing, mobile armoring, or the temporal lag between stage and bedform growth. Ψ reveals along-stream variations in hysteresis for each storm, with a peak in hysteresis further downstream for the second event. The pattern is consistent with a migrating sediment pulse that is a predicted consequence of the dam removal. Our results indicate that hysteresis in the relationship between seismic wave amplitude and river stage may track sediment transport.

1. Introduction

Understanding when and at what rate coarse sediment moves is key to predicting river channel change. Current approaches to predicting or estimating transport rates include in situ measurements (e.g., Reid et al., 1985) and empirically calibrated relationships (e.g., Wilcock and Crowe, 2003; Meyer-Peter and Müller, 1948). In situ measurements are labor intensive and often logistically challenging and consequently only available for a limited number of small streams. Idealized empirically calibrated relationships, in turn, may be of limited application given the complexity of real rivers. The difficulties with both of these approaches are exacerbated in extreme events, when taking measurements becomes more challenging and dangerous, and empirical relationships are even less representative. However, the importance of events scales with these difficulties: sediment transport is nonlinear, so larger events have a relatively greater impact on river systems (Parker, 2005).

Several new technologies present promising approaches to measuring bedload sediment transport. Geophone plate installations and hydrophones have both been used very successfully in studies of bedload sediment transport (e.g., Rickenmann and McArdell, 2007; Turowski et al., 2009; Bogen and Møen, 2003). However, attaching geophones beneath steel plates embedded in streambeds requires expensive large-scale installations. Hydrophones, while more easily deployable, risk instrument damage or loss due to their placement in the flow itself. Both approaches also potentially disrupt fluid flow or bedload transport. Fluvial

* Tel.: +1 858 337 4782.
E-mail address: dlroth@ucsc.edu (D.L. Roth).

http://dx.doi.org/10.1016/j.epsl.2014.07.019

seismology is one attractive option for quantifying bedload transport directly in a natural setting from outside the channel itself. Elastic waves generated by particle-bed impacts can be measured with standard seismic equipment located on the river banks. Analysis of these waves shows promise in constraining bedload transport and bed evolution. Burtin et al. (2008) demonstrated that a large river was a major source of high frequency (1–20 Hz) ambient seismic noise in the Himalayas, and later showed that high frequency noise was likely attributable to bedload sediment transport (Burtin et al., 2010). A key observation was a seasonal variation in the seismic response for a given discharge, termed hysteresis.

Hsu et al. (2011) explored the time evolution of seismic amplitude as a function of stage over the course of single storm events in a gravel-bed river in Taiwan, and found a consistent clockwise hysteresis in all events. They proposed that this relationship represented a decrease in transport efficiency over the storm, which could be explained by a temporal evolution of the bed surface during storms. Schmandt et al. (2013) found a similar hysteresis in a restricted frequency band during a flood of the Colorado River at a site proximal to easily mobilized coarse sediment.

Similar hysteresis effects are observed in studies directly measuring bedload transport in gravel-bed rivers (e.g., Humphries et al., 2012). Hysteresis in the relationship between sediment transport rate and some measure of flow strength occurs over a wide range of timescales (hours to years), and in both clockwise (higher transport on rising limb) (e.g., Allen, 1974; Nanson, 1974; Walling, 1977; Dunne and Leopold, 1978; Moog and Whiting, 1998) and counterclockwise (higher transport on falling limb) (e.g., Milhous and Klingeman, 1992; Klingeman and Emmett, 1982; Emmett et al., 1983) directions. The cause of hysteresis is argued to reflect changes in sediment supply (e.g., Nanson, 1974; Reid et al., 1985) or time-dependent evolution of the bed, such as armoring, packing, roughening, or coarsening (e.g., Milhous and Klingeman, 1992; Dietrich et al., 1989). Thus, while the absence of hysteresis in seismic amplitudes may not necessarily indicate an absence of sediment transport, the presence of seismic hysteresis may plausibly indicate the presence of transport in gravel rivers where the above mechanisms operate.

Although several studies demonstrate the potential for measuring bedload transport from seismic hysteresis, the lack of independent constraints limits this method's implementation. Here we explore this potential by comparing high-frequency broadband seismic data from stations along the Chijiawan River in Taiwan, following the removal of a 13 m check dam in 2011. This field site was selected for two reasons. First, sediment transport occurs primarily during episodic summer typhoons, which is ideal for examining hysteresis over individual transport events. Second, a dam removal produces rapid and distinctive changes in bedload transport patterns in both time and space, which we independently constrain through repeat surveys and field observations. We can thus compare the spatiotemporal evolution of both sediment transport rates and seismic hysteresis in response to the dam removal.

Previous studies of coarse sediment released following dam removal (Cui et al., 2003; Sklar et al., 2009) or landsliding (Sutherland et al., 2002) indicate that sediment moves in a pulse-like wave, combining advection and diffusive spreading downstream. Flume experiments indicate that advection is favored only when the volume of introduced sediment is small compared to channel dimensions (i.e., unable to cover the entire flume bed) (Sklar et al., 2009). Otherwise, dispersion of introduced sediment appears to be dominant (Cui et al., 2003; Sutherland et al., 2002; Sklar et al., 2009). We therefore predict that later floods should produce higher transport rates farther down from the dam and along a larger reach of the river as the sediment pulse disperses. Thus, in addition to further validating the use of seismic waves to measure bedload transport, this experiment provides rare constraints on sediment pulse transport following a medium sized dam removal in a steep river.

In Section 2, we introduce the field site, study design, and event chronology. In Section 3, we discuss river elevation, water depth and seismic data collection, as well as preliminary processing methods for these data. Section 4 details the analysis used to infer sediment transport patterns from topography and seismic hysteresis. Section 5 describes the evidence that the signal of bedload sediment transport is embedded in seismic amplitudes and that we appear to be tracking a migrating sediment pulse. In Section 6, we discuss the significance of our results and potential causes of hysteresis in the relationship between seismic amplitude and river stage, and suggest time-dependent evolution of the bed as its likely mechanism.

2. Field site, study design and chronology

We collected seismic data for 6 months following the late May, 2011 removal of a 13-m high dam on the Chijiawan River in Shei-Pa National Park in northern Taiwan (Fig. 1a). The catchment upstream of the study site ranges in elevation from 1700 to 3800 m a.s.l., and has mean annual precipitation of 2–3 m/yr. The mean channel slope of the study reach is ∼2%, with a drainage area of 50.3 km^2 at the check dam.

Eight Guralp CMG-6TD broadband seismometers were installed along a ∼3 km, south-flowing reach of the river (Fig. 1b), from May to mid-November, 2011. All seismometers sampled at either 100 or 200 Hz and were installed within ∼ 50 m of the river to minimize attenuation of higher frequencies. Station HGB was installed directly on a bedrock exposure; all other seismic stations were on alluvial terraces.

The underlying bedrock in this region consists of slate interbedded with quartzite, and bedload is primarily quartzite. The study reach is a mixed bedrock-alluvial channel that traverses a bedrock gorge 40 m to 370 m downstream of the dam.

The main stage recorder was a downlooking bridge-mounted radar depth gauge (SITRANS Probe LR) located on a bedrock reach approximately 240 m downstream of seismic station (HGB). Two storms (June 24–26 and October 2–11, 2011) were selected for comparison due to nearly identical maximum stages of ∼ 1.5 m. Not included in the seismic analysis for this study were two minor discharge events (<0.75 m) that occurred between the June and October storms.

3. Data collection methods

We constrain the events following the dam removal from field observations, elevation long profiles, gauge recordings of stage, and seismic recordings of ground motion.

3.1. Field observations

Field observations before and after each storm independently constrained patterns of sediment transport along the river during each storm. These patterns were determined through field observation, repeat photographs (Fig. 2a) of several reaches taken before, during and after each storm, and monitoring of erosion, deposition and aggradation at marker holes drilled in the bedrock as fixed spatial reference points along the channel bed and banks adjacent to the seismic stations.

3.2. Elevation long profiles

Channel bed or water surface elevation was surveyed six times throughout the season. Table 1 shows the date and method of each

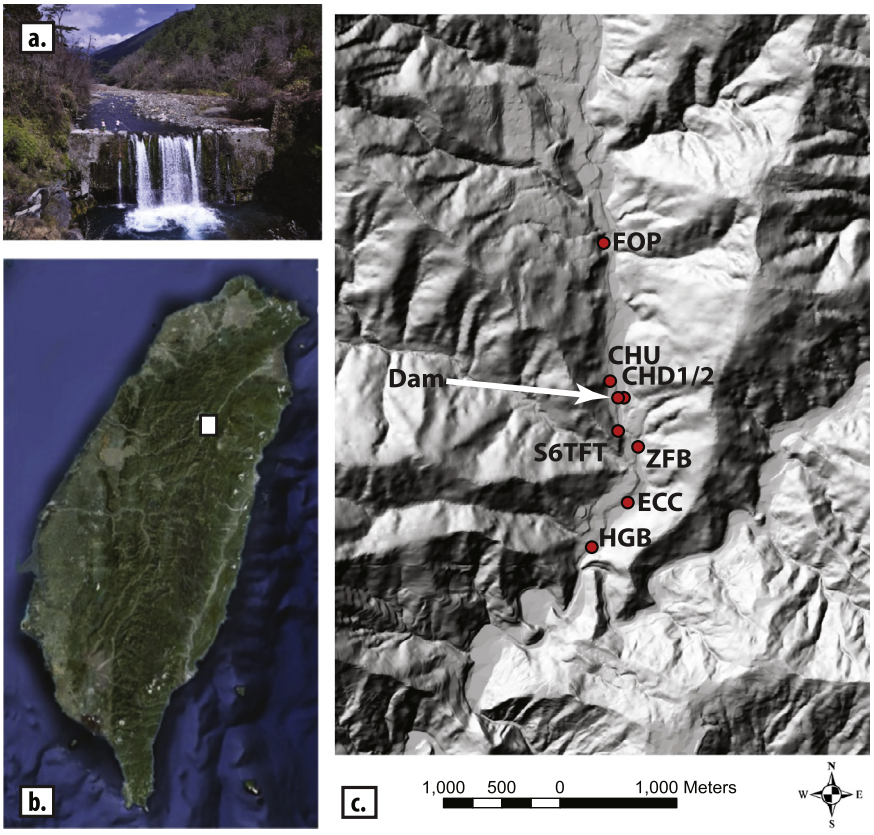

Fig. 1. (a) Dam, (b) field site location in Taiwan, and (c) shaded relief map of field site with seismic stations. CHD1 and CHD2 are directly adjacent to the check dam, but at different distances from the river; the more distant site (CHD2) was not included in this study's seismic hysteresis analysis.

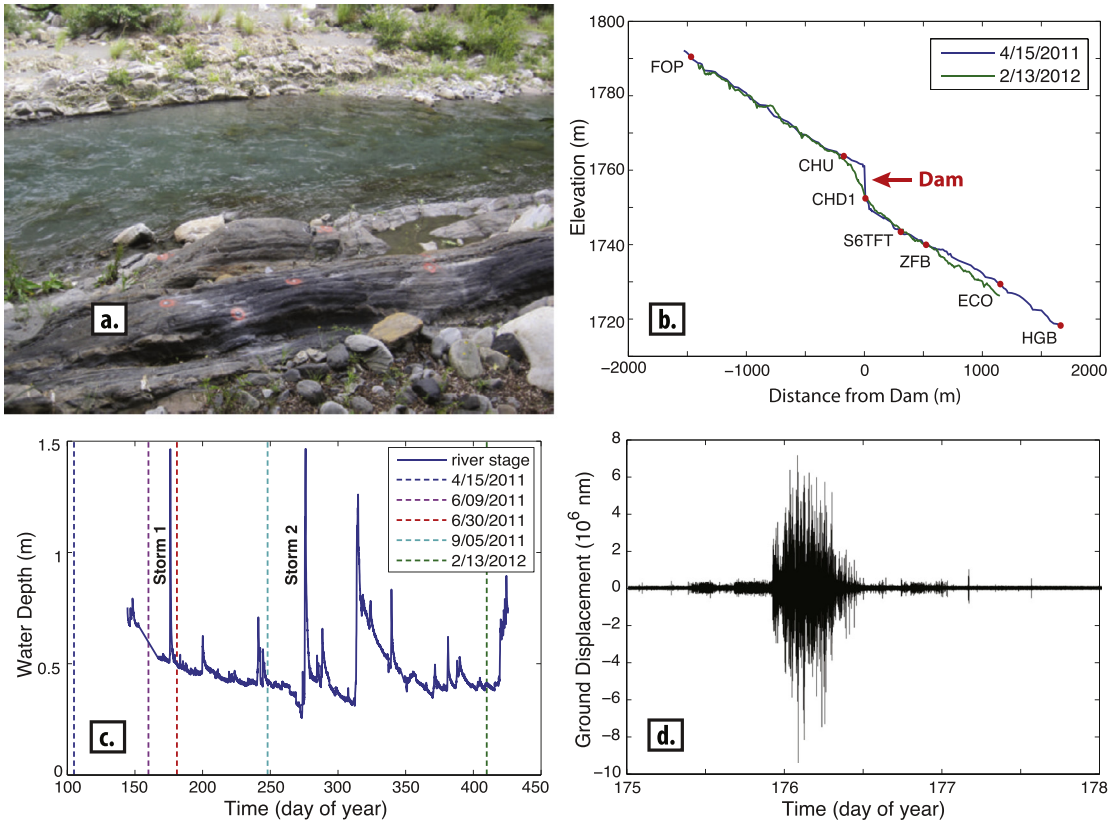

Fig. 2. Examples of each raw data type used for sediment transport analysis. (a) Photograph near station HGB showing reference marker holes used to track sediment erosion and deposition. (b) River elevation long profiles taken 4/15/2011 (before the dam was removed) and 2/13/2012 (after the typhoon season), and positions of all seismic stations. (c) River stage data for the entire field season, with dates of elevation long profiles used in this study, Storm 1 and Storm 2 marked for reference. (d) Seismogram showing the vertical component of ground motion at station CHD1 during Storm 1.

Table 1
Elevation long profiles.

Date	Surface surveyed	Method
4/15/11	water surface	RTK GPS
6/9/11	bed thalweg	Virtual Reference Station
6/30/11	bed thalweg	Leica FlexLine TS02 total station
7/26/11	bed thalweg	Leica FlexLine TS02 total station
9/5/11	bed thalweg	Leica FlexLine TS02 total station
2/13/12	bed thalweg	Leica FlexLine TS02 total station

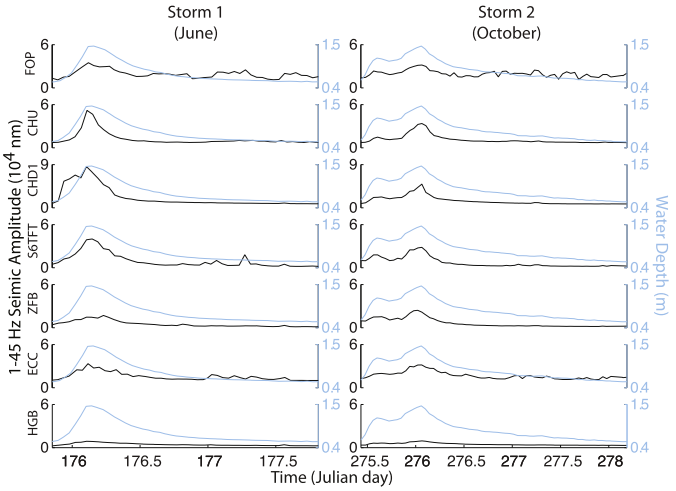

Fig. 3. Water level (blue) and seismic amplitude (black) in the 1–45 Hz band, over both storms at all stations in downstream order. (For interpretation of the references to color in this figure legend, the reader is referred to the web version of this article.)

survey. Fig. 2b shows two example elevation long profiles, taken April 15, 2011 before the dam was removed, and February 13, 2012, following the typhoon season and all transport reported here.

3.3. Gauge data

Radar gauge data were taken at 5-min intervals, corrected for bed elevation change measured beneath the gauge (see Supplementary Section 1) and averaged into hourly values. Fig. 2c shows all hourly gauge data throughout the season, with the dates of all elevation long profiles used in this study, Storm 1 and Storm 2 marked for reference.

Storm beginning times were identified visually using gauge data, and the first storm's ending was defined as the time at which stage returned its initial value. The second storm's ending was chosen to exclude a small secondary surge in stage that occurred before the stage fully returned to its pre-storm level.

3.4. Seismic data

We focus on the vertical (z) component of ground motion, which is argued to correlate with bedload transport. Burtin et al. (2010) indicated that bedload transport in the trans-Himalayan Trisuli River correlates most strongly with Rayleigh surface waves and/or S waves. Tsai et al. (2012) attributed this observation to the nearly vertical nature of impacts, and modeled Rayleigh waves as the predominant elastic waves generated by saltating bedload transport.

Hourly bandpass envelopes measuring the signal's power over time within the 1–45 Hz frequency band were calculated from raw daily seismic data (see Supplementary Section 2), and cross-interpolated with hourly gauge data. Fig. 3 shows hourly stage and seismic amplitude over the course of each storm at each station.

4. Sediment transport analysis: methods

Identifying sediment transport patterns requires two metrics: one based on topographic data and another based on seismic data. Below, we describe those metrics individually before returning to the full dataset to evaluate the effects of the storms.

4.1. Apparent sediment flux q_A

4.1.1. Measurement of q_A profiles

Mass conservation dictates that changes in bed elevation over time, $\frac{dz}{dt}$, should scale negatively with the downstream gradient of volumetric sediment flux per unit channel width, $\frac{dq_b}{dx}$ (Exner, 1920, 1925):

$$\frac{dz}{dt} \propto -\frac{dq_b}{dx} \tag{1}$$

This relationship implies that differenced 1D elevation profiles (e.g., Fig. 2b), can be used to calculate an apparent sediment flux $q_A(x, \Delta t)$ describing the total apparent volume of sediment per unit channel width (assumed to be constant) that moved past position x over the time between the profiles (e.g., Church, 2006).

$$q_A(x, \Delta t) = C - \frac{\sum_{x_0}^{x} \Delta z_x \Delta x}{\Delta t} \tag{2}$$

Elevation change Δz_x was calculated at each point x along the river by interpolating and differencing a pair of smoothed profiles. The apparent flux $q_A(x, \Delta t)$ for that period was found at each position x by summing the elevation change (Δz_x) times the spacing Δx over all positions from x_0, the farthest upstream point common to all profiles, to x. We then normalized by a proxy for active transport time (Δt) within each period: the time during which the stage was above a curve fit to the base flow level. The integration constant, C, includes any initial sediment input from upstream of reference point x_0. We neglect this unconstrained constant in our calculations.

We calculated this apparent flux for three periods (Supplementary Fig. 1): April 15–June 9 (pre-dam removal up to Storm 1), June 9–June 30 (Storm 1, June 24-26), and June 30–Sept. 5 (two minor discharge events between Storms 1 and 2). We were unable to show apparent flux over Storm 2 (Oct. 2–11) because no elevation long profiles were taken after Sept. 5 for a period of 5 months, during which several other large transport events occurred (Fig. 2c).

4.1.2. Uncertainty in q_A profiles

The reference point, x_0, determined by the upstream extent of the elevation long profiles, excludes sediment input from any portion of the sediment pulse, or other external sources, upstream of x_0. This introduces an arbitrary offset to q_A equal to the neglected integration constant C in Eq. (2).

Our calculations also assume constant channel width, although it can evolve dynamically after dam removals (e.g., Cantelli et al., 2004). In addition, the bedrock gorge downstream of the dam may have constricted deposition of sediment eroded from wider channel cross-sections upstream, leading to an imbalance between measured erosion and aggradation rates and a spurious decrease in apparent flux in this region.

Fitting the threshold stage for active transport with the base flow level assumes that the critical shear stress to initiate transport evolved over the field season. While this assumption may be reasonable (e.g., Buffington and Montgomery, 1997; Charru et al., 2004), the exact magnitude of that evolution is unknown. We also lack gauge data for much of April 15–June 9 (Fig. 2c), so the active

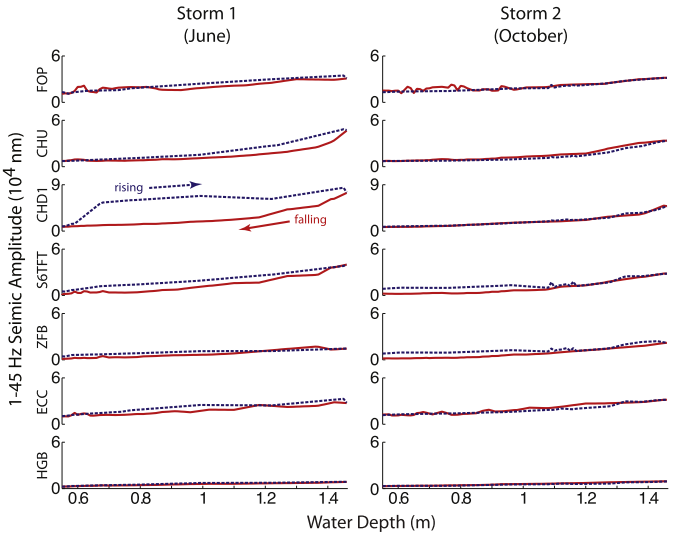

Fig. 4. Seismic amplitude as a function of concurrent water depth at each station over both storms. Stations are listed in downstream order. Blue and red lines show rising and falling water levels, respectively. The data from the dam station (CHD1) shows a large difference in hysteresis over the first and second storms. (For interpretation of the references to color in this figure legend, the reader is referred to the web version of this article.)

transport time within this period is speculative; however, it is unlikely that transport occurred before the dam removal in late May. Our approach may thus result in erroneous Δt values in Eq. (2).

Finally, unaccounted lateral sediment sources and sinks, and variations in the locations and methods used to measure elevation also contribute to uncertainty in the apparent flux data.

Due to these factors, we choose to refer to our measurements as "apparent" sediment flux. We present these apparent profiles as an index of spatial gradients in sediment transport along the river over time.

4.2. Normalized seismic hysteresis metric Ψ

4.2.1. Measurement of Ψ

The standard definition of hysteresis describes the area between the increasing and decreasing limbs of the response curve for a memory- or state-dependent system. Similarly, we define a seismic metric, Ψ, to quantify hysteresis in the relationship between seismic amplitude and water depth during each storm at each station by finding a normalized area within the seismic amplitude versus water depth curve. For each storm, gauge and seismic data were divided into 'rising' and 'falling' limbs (see Supplementary Section 3). Fig. 4 shows the seismic amplitude at each station as a function of water depth over both storms.

The seismic amplitudes at each station cannot thus far be interpreted directly in terms of bedload transport for two reasons. First, the amplitudes contain an additional component generated by water turbulence. Second, the measured signal has been attenuated by a different amount at each station. Because seismic waves attenuate as a function of path length, seismic amplitudes registered at a given station are dependent on both the source–receiver distance and the substrate-dependent attenuation factor over that distance.

At any given flow depth d, the seismic amplitudes on the rising and falling limbs ($y_{rise,d}$ and $y_{fall,d}$) are thus a combination of the signals generated by rising or falling bedload sediment transport ($B_{rise,d}$ and $B_{fall,d}$) and water (W_d), and some frequency- and distance-dependent attenuation function (A). For a single frequency,

$$y_{rise,d} = A(B_{rise,d} + W_d)$$

$$y_{fall,d} = A(B_{fall,d} + W_d). \quad (3)$$

The complex attenuation factor A integrates effects across the whole channel and is unknown. Eq. (3) thus comprises an underdetermined system of equations, from which we can remove only one unknown variable. We assume the signal of water, W_d, is approximately constant between stations, and design a metric that is insensitive to attenuation.

To cancel the attenuation terms, the area between each rising and falling limb was normalized by the area under the falling limb (Fig. 4). The normalized hysteresis, Ψ, is

$$\Psi = \frac{\sum_{d_{\min}}^{d_{\max}}(y_{rise,d} - y_{fall,d})}{\sum_{d_{\min}}^{d_{\max}} y_{fall,d}} = \frac{\sum_{d_{\min}}^{d_{\max}}(B_{rise,d} - B_{fall,d})}{\sum_{d_{\min}}^{d_{\max}}(B_{fall,d} + W_d)}, \quad (4)$$

where each curve has been summed over all average hourly stage values through the storm from $d_{\min} = 0.55$ m to the peak depth of $d_{\max} = 1.5$ m.

Thus, the hysteresis metric Ψ is simply the fractional change between average rising and falling limb seismic amplitudes over a given storm. $\Psi > 0$ and $\Psi < 0$ respectively indicate net clockwise and counterclockwise hysteresis. Ψ is insensitive to gauge averaging intervals (Supplementary Figs. 2 and 3) and demonstrates similar patterns with several variations on Eq. (4) (Supplementary Fig. 4).

4.2.2. Sources of uncertainty in normalized seismic hysteresis metric Ψ

Measurement error

Error bars on Ψ indicate the amount of spurious hysteresis that would have been produced at each site by 10 cm of uncorrected erosion at the gauge (see Supplementary Section 4). We interpret only values outside this range as representing true changes in the relationship between seismic amplitude and stage.

Uncertainty from normalization

Using normalization to account for attenuation assumes that both the attenuation factor and source–receiver distance for each station remains constant between storms. If evolution of the riverbed or migration of the thalweg (the deepest point of the channel at a given cross-section) significantly alters the attenuation factor or source–receiver distance, this approach may not fully account for attenuation. Additionally, we neglect the frequency-dependence of attenuation: higher frequencies attenuate more strongly with distance, so high frequency energy from the nearest points on the river may dominate stations closer to the river. As distance from the river increases, these higher frequencies will attenuate so the nearest source points cease to dominate. Seismic stations farther from the river may thus effectively register signals integrated over a longer reach of the river, producing inconsistency between stations. The supplementary material (Supplementary Fig. 4) includes a comparison of different normalizations of Ψ at the check dam station (CHD1) and a second station (CHD2) farther away from the river, but at the same longitudinal transect. Normalization by the falling limb (Eq. (4)) was selected to minimize the difference in Ψ at these stations, which we consider a proxy for the overall sensitivity of Ψ to distance.

5. Sediment transport analysis: observations

We now return to the full dataset to determine the transport patterns in each storm. We compare field observations with our metrics for apparent flux and seismic hysteresis to find commonalities and track the sediment pulse released by the dam removal.

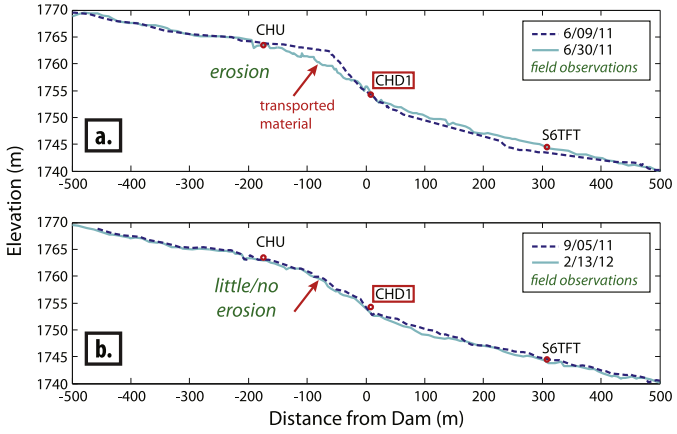

Fig. 5. Elevation long profiles near the dam, bracketing (a) Storm 1, and (b) Storm 2; significantly more material was removed from the knickpoint and transported past the dam station (CHD1) in Storm 1 than in Storm 2. This finding is also supported by field observations (green). (For interpretation of the references to color in this figure legend, the reader is referred to the web version of this article.)

5.1. Field observations

In the early stages of Storm 1, the channel upstream of the dam widened primarily by bank collapse (Supplementary Fig. 5a, b and c). Over the storm, the gravel knickpoint was eroded down to the remaining, concrete lower portion of the dam, which was left in place after the dam removal (Supplementary Fig. 6). Deposition of the eroded material occurred between the dam and the ZFB station (Wang and Kuo, submitted for publication) (Supplementary Fig. 7). Negligible deposition and transport occurred at the farthest downstream stations (ECC and HGB) (Supplementary Fig. 8).

Storm 2 produced little elevation change at the dam (Supplementary Fig. 5d). The region immediately below the dam and downstream to the S6TFT and ZFB stations, where deposition occurred in Storm 1, showed evidence of transport, but no further aggradation (Supplementary Fig. 9). At the farthest downstream stations (ECC and HGB), minor transport but no changes in channel form (i.e., aggradation or erosion) were observed.

Based on these observations, we infer that the first storm induced massive transport at the dam, as loose sediment from behind the dam left the knickpoint in a pulse whose front edge reached the S6TFT and ZFB stations by the end of the storm. In the second storm, relatively little sediment was sourced from the knickpoint and the pulse was advected further downstream, with the bulk of it transported past the S6TFT and ZFB stations but the leading edge upstream of stations ECC and HGB. We speculate that the absence of further erosion at the knickpoint, despite its relatively steep local slope, was due to the base-level control provided by the remaining bottom of the dam.

5.2. Change in transport at the dam

5.2.1. Change in elevation long profiles

Fig. 5 shows close-ups of the elevation long profiles near the dam, before and after each storm, with seismic stations marked for reference. These profiles are consistent with our qualitative field observations (also shown in green) and indicate that more transport occurred at the dam over the first storm than the second. Fig. 5a shows that knickpoint material was transported past the seismic station at the dam (CHD1) during the first storm. While the second storm (5b) caused some incision downstream of the dam, the knickpoint itself experienced negligible erosion compared to the first storm. This difference is surprising because the profiles in Fig. 5b spanned five months and a third storm. Again, we speculate that the apparent change in transport efficiency resulted from the base-level control provided by the remaining lower portion of the cement dam.

5.2.2. Change in seismic hysteresis

The difference in transport observed between the two storms is also evident in the seismic data (Fig. 4). The station closest to the dam (CHD1) displays a large amount of hysteresis in the first storm, when the dam experienced significant transport, but negligible hysteresis during the second storm with very little inferred transport. This systematic behavior is consistent with hysteresis at this site being produced by sediment transport.

5.3. Sediment pulse advection and diffusion

5.3.1. Transport patterns from apparent sediment flux q_A

The apparent flux profiles are shown in Fig. 6a, b, d. We report the maximum amplitudes of each curve rather than the absolute values due to the arbitrary offset from the integration constant C in Eq. (2). Profiles 6a and 6b demonstrate what we speculate to be a spurious decrease in apparent flux below the initial upstream values. As mentioned in Section 4.1, a change in downstream channel width due to constriction in the bedrock gorge could explain this trend. Field observations confirm that aggradation occurred within the gorge during both of these periods. Additionally, sediment input due to the channel widening via bank collapse upstream of the dam is not reflected in the elevation profiles, and the reference point x_0 may not cover the upstream extent of vertical incision into the knickpoint. After Storm 1, erosion in this region decreased due to the downstream migration of pulse material and knickpoint stabilization, which may explain the lack of similar decrease in the third profile, Fig. 6d. Again, we emphasize the shapes of these profiles simply as indices of sediment transport along the river.

As such, these apparent flux profiles agree broadly with field observations and provide further confirmation that sediment transport patterns evolved as expected: the peak in transport occurs first at the point of highest convexity at the dam (Fig. 6a), then shifts slightly upstream with the propagating knickpoint (Fig. 6b), while transport of the sediment pulse proceeds downstream in a pattern consistent with a combination of advection (bulk downstream movement) and dispersion (downstream spreading) (Fig. 6a, b and d).

5.3.2. Transport patterns from seismic data: normalized hysteresis metric Ψ

The normalized hysteresis Ψ is shown at each seismic station over both storms in Figs. 6c and 6e. The highest rate of apparent sediment transport is spatially coincident with the peak in Ψ at the check dam station (CHD1) during the first storm, followed by a downstream decrease to station ZFB, the inferred downstream extent of the pulse. The downstream translation and dispersion of the sediment pulse over time is demonstrated in the second storm: Ψ decreases at the dam, and the peak in Ψ moves farther downstream, decreases in amplitude, and spreads over two stations. Our inferences of sediment transport patterns based on field observations (Fig. 6) further corroborate the trends in Ψ: regions where transport was known to have occurred match regions with high Ψ, and regions with low transport match regions of low Ψ.

6. Discussion

6.1. Does Ψ scale with bedload transport?

Ψ is a numerical measurement of the fractional hysteresis in seismic signals, but the exact nature of the scaling between Ψ and sediment transport rates is undetermined; this scaling is likely

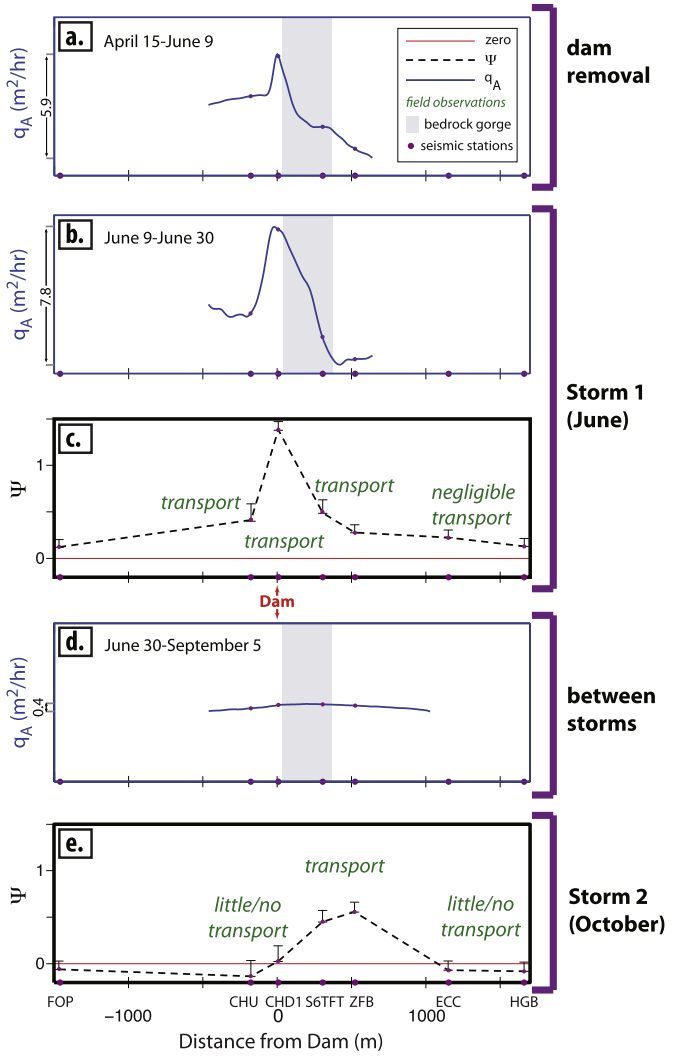

Fig. 6. The sediment pulse released from the dam can be tracked through both the normalized hysteresis metric, Ψ (black), and the magnitude of apparent sediment flux profiles, q_A (blue), shown jointly in chronological sequence (a) over the dam removal, (b and c) during Storm 1, (d) between the storms, and (e) during Storm 2. Seismic stations are marked for reference. Ψ corresponds with the contemporaneous apparent flux profile over Storm 1, and with field observations (shown in green) over both storms; apparent flux profiles and Ψ also clearly demonstrate corroborating patterns of downstream advection and diffusion of the sediment pulse over time. Error bars on Ψ represent simulated corrections for artificial hysteresis that would be produced by a −10 cm offset in flow depth (Supplementary Section 4). Error bars that cross zero indicate that hysteresis may be a spurious artifact of uncorrected erosion at the radar gauge site, rather than actual changes in the relationship between seismic amplitude and flow depth. (For interpretation of the references to color in this figure legend, the reader is referred to the web version of this article.)

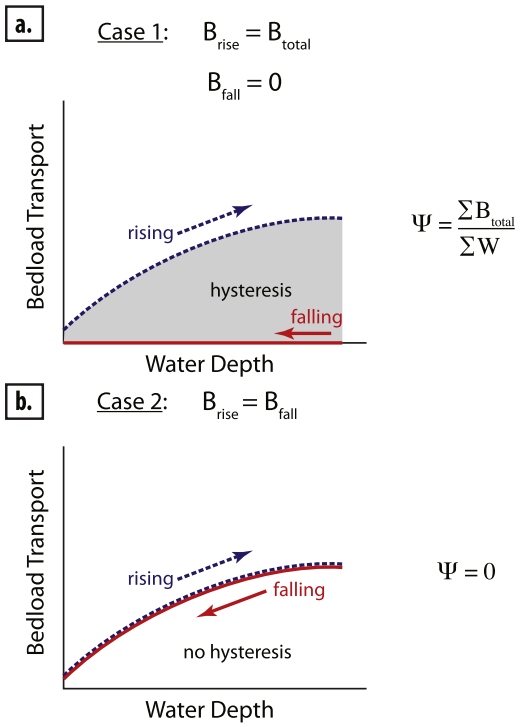

Fig. 7. Two end-member cases illustrating the sensitivity of Ψ (Eq. (4)) to the ratio of rising-to-falling limb transport throughout a flood. B_{rise} and B_{fall} are the components of the seismic signal generated by bedload transport on the flood's rising and falling limbs, B_{total} is the total signal of all bedload transport, and W is the signal generated by water. (a) Case 1: All bedload transport occurs on the rising limb and the falling limb generates no transport signal, producing hysteresis. (b) Case 2: Transport occurs at equal rates on the rising and falling limbs, producing no hysteresis.

to vary between locations and even evolve over time at a single site. We therefore use Ψ only as a qualitative metric for relative transport rates over time and between stations. Below, we clarify this implementation by showing that Ψ does generally scale with bedload (albeit in a quantitatively unknown way), and discussing factors that may influence that scaling.

The use of seismic hysteresis as an index for sediment transport relies on unequal amounts of transport on the rising and falling limbs of a flood, as well as the assumption that relative rates of bedload transport produce proportionally consistent relative values for bedload-generated seismic signals (i.e., the ratio of rising-to-falling limb transport rates at flow depth d is equal to the ratio $B_{rise,d}/B_{fall,d}$). By normalizing hysteresis by the falling limb signal (Eq. (4)), we further interpret hysteresis only in terms of proportional differences in rising and falling limb amplitudes, rather than absolute differences. The accuracy of Ψ in representing changes in the magnitude of sediment transport (Fig. 6) is therefore dependent on the ratio of transport occurring on the rising and falling limbs of a given storm, the dynamic scaling of that ratio with overall transport, the magnitude of the transport signal relative to the water signal, and the uniformity of these factors between stations and over time.

Consider the two end-member cases illustrated by the cartoons in Fig. 7. (1) All transport occurs on the rising limb ($B_{fall,d} = 0$, and $B_{rise,d} = B_{total,d}$), and the falling limb signal is entirely generated by water (Fig. 7a): the ratio of rising-to-falling limb transport approaches infinity and becomes highly sensitive to overall transport since increases in transport solely affect the rising limb amplitude. In this case, Ψ in Eq. (4) represents the total signal of bedload transport over the storm, normalized by the water signal ($\Psi = \sum B_{total,d} / \sum W_d$). Assuming the water signal ($\sum W_d$) is similar between stations or times, a change in Ψ would thus indicate an equivalent proportional change in total transport ($\sum B_{total,d}$). (2) Transport occurs equally on the rising and falling limbs ($B_{rise,d} = B_{fall,d}$) so the ratio is constant and insensitive to transport (Fig. 7b): this produces no hysteresis, and Ψ is completely unrepresentative of transport rates ($\Psi = 0$). Between these end-member examples, as the ratio of transport on the rising limb increases toward Case 1, the amount of hysteresis also increases and becomes more representative of actual bedload transport rates. Similarly, as that ratio's sensitivity to overall transport increases toward Case 1, the accuracy of the normalized fractional hysteresis Ψ increases.

At any constant ratio aside from equal transport (Case 2), however, under most circumstances Ψ will still scale with bedload to some extent. To demonstrate this, assume the rising limb bedload

signal ($B_{rise,d}$) is a constant ratio R of the falling limb bedload signal ($B_{fall,d}$), such that $B_{rise,d} = RB_{fall,d}$. Substitution into the right side of Eq. (4) yields

$$\Psi = \frac{\sum_{d_{\min}}^{d_{\max}} B_{fall,d}(R-1)}{\sum_{d_{\min}}^{d_{\max}} (B_{fall,d} + W_d)}. \quad (5)$$

In the limiting case that $\sum B_{fall,d} \gg \sum W_d$, then $\sum(B_{fall,d} + W_d) \approx \sum B_{fall,d}$ and the fractional hysteresis Ψ becomes approximately constant:

$$\Psi \approx R - 1 \quad (6)$$

Thus, when the bedload signal is very large with respect to the water signal, Ψ becomes insensitive to changes in bedload. However, because bedload transport occurs only during elevated flow rates, it is unlikely that the water signal can be neglected, especially in highly turbulent flows.

6.2. Interpretations of hysteresis

Below we discuss the contribution of water turbulence to the seismic signal, potential physical origins of the clockwise hysteresis and its insensitivity to the position of the sediment pulse. We also entertain alternative explanations for the hysteresis due to processes unrelated to sediment transport.

6.2.1. The signal of water turbulence

Field observations (Supplementary Figs. 5c and 5d) revealed little to no coarse sediment transport at the dam during the second storm. Thus this station's seismic signal in Storm 2 represents primarily water turbulence, the magnitude of which we assume to be similar on the rising and falling limbs of the storm (e.g., Schmandt et al., 2013). A significant component of the seismic amplitude therefore reflects processes other than sediment transport. This highlights the utility of hysteresis as a means of distinguishing the sediment transport component from the water component of seismic amplitudes.

6.2.2. Physical origins of the clockwise hysteresis

We consistently observe net clockwise hysteresis at all sites in both storms. Because the largest component of the sediment source is assumed to be the migrating pulse from the dam, this observation provides some insight into possible physical mechanisms causing the hysteresis. This is best illustrated by a simple thought experiment: how might we expect Ψ to behave if sediment transport increased purely as a function of discharge and sediment supply? The sediment pulse may be roughly modeled as a boxcar traveling downstream, such that a given point on the river will see a change in sediment supply with the arrival or departure of the pulse. This scenario would lead to higher rates of transport at a given stage after the pulse arrives or before it departs. If the pulse arrives but does not depart during a single storm, we expect that site to experience less transport at a given stage on the storm's rising limb (before the pulse's arrival increases local sediment supply) than at the same stage on the falling limb (when supply is higher). This would result in counter-clockwise hysteresis in both the sediment rating curve and seismic data. The pulse's departure and subsequent decrease in sediment supply could similarly be expected to produce lower transport rates at a given stage on the storm's falling limb, or clockwise hysteresis.

Based on both field observations and the apparent flux profiles, the front edge of the sediment pulse arrived at sites S6TFT and ZFB during the first storm. However, Fig. 6c shows no counter-clockwise (negative) hysteresis at these sites. In fact, these sites show significant clockwise (positive) hysteresis, indicating that transport was actually lower on the falling limb although the available coarse sediment supply was higher. It therefore appears that the expectations in our thought experiment are incorrect: the pulse's arrival does not lead to an increase in transport on the falling limb. This implies that the physical mechanism generating hysteresis is producing consistently lower sediment transport rates on the storms' falling limbs, regardless of changes in sediment supply relative to the rising limb. Thus, while the exhaustion of sediment supply has commonly been cited as a major cause of hysteresis in bedload transport (e.g., Nanson, 1974; Reid et al., 1985; Whiting et al., 1999), it appears not to be the dominant mechanism at work here.

This finding is similar to experimental flume results from Humphries et al. (2012), who modeled the downstream motion of a coarse sediment pulse under a time-varying hydrograph. Transport at a given discharge was invariably higher on the rising limb than the falling limb, leading to a well-defined clockwise hysteresis over all hydrographs, regardless of the pulse's position in time and space relative to the transport observation point. The only exception was the peak in sediment transport itself, which coincided with the increase in sediment supply due to the arrival of the main portion of the pulse (analogous to our simple boxcar model), and hence occasionally occurred after the discharge peak. The otherwise consistent decrease in falling limb transport and corresponding clockwise hysteresis found by Humphries et al. (2012) mirrors our own observations of Ψ. Humphries et al. (2012) attributed the dominance of clockwise hysteresis to two mechanisms.

The first mechanism is the time-lag between discharge and the growth or decay of bedforms (e.g., Martin and Jerolmack, 2013). Increases in form drag due to bedform roughness should decrease the bed shear stress available to entrain particles. Thus for a given stage, the bed will tend to be smoother and more able to move sediment on the rising limb than the falling limb. While bedforms like dunes are generally rare in gravel-bed rivers, several studies show that they can form during large floods and cause hysteresis in bedload transport (e.g., Kuhnle, 1992; Griffiths and Sutherland, 1977; Bell and Sutherland, 1983; Lee et al., 2004).

The second hysteresis inducing mechanism observed by Humphries et al. (2012) was a coarsening of bedload on the rising limb (implying fining or un-armoring of the bed) and fining of bedload on the falling limb (implying armor formation or coarsening on the bed). If bed fining and coarsening (and the inferred armor removal and formation) is the process driving hysteresis, then Humphries et al. (2012) interpretation implies that for a given stage the bed must be finer on the rising limb than the falling limb, indicating asymmetry in the fining/coarsening (or armor mobilizing/forming) mechanism. Armor formation over a single storm is a relatively undocumented phenomenon due in part to the difficulty in measuring it, but other studies of gravel-bed rivers have seen results similar to Humphries et al. (2012) in flows high enough to mobilize bed armor (e.g., Kuhnle, 1992; Whiting et al., 1999).

Other possible contributors to the observed clockwise hysteresis include progressive packing and coarsening of the bed over time. Packing of grains on the bed can inhibit mobility by increasing entrainment stress (e.g., Charru, et al., 2004). This produces clockwise hysteresis by decreasing transport efficiency for a given stress. In cases where sediment supply is small relative to transport capacity, coarsening of the bed can occur due to selective transport of small grains (e.g., Dietrich et al., 1989). This leads to clockwise hysteresis by decreasing the number of grains available for entrainment at a given stress. Wohl and Cenderelli (2000) observed this coarsening effect following a reservoir sediment release: beginning with upstream sites and progressing farther downstream over time, the channel became sediment supply-limited, first with respect to small grains, then larger grains. A similar grain-size-

dependent supply limitation could have occurred downstream of the Chijiawan dam.

Lacking detailed data on sediment transport rates, grain sizes and bed evolution for this study, we can only speculate about the physical mechanism(s) producing the implied hysteresis in bedload transport rates. That said, as detailed above, temporal changes in sediment supply do not appear to strongly influence the direction of hysteresis; they do, however, appear to strongly influence the magnitude of clockwise hysteresis. As per Section 6.1, the scaling of Ψ with inferred transport rates following the position of the sediment pulse has two possible implications. First, if the ratio of rising to falling limb transport is constant, the bedload component of the signal may not be significantly large enough to dominate over the water component, resulting in a non-constant ratio of the total rising and falling limb signals. Second, the ratio of rising to falling limb transport may actually scale with overall transport, suggesting a rate-dependence between transport and whatever mechanism is causing transport to decrease on the falling limb. We find it most likely that time-dependent evolution of the bed, such as grain packing, asymmetric fining and coarsening of the bed with stage (possibly due to mobile armoring), or the temporal lag between stage and bedform adjustment, is responsible for the hysteresis.

Ultimately, however, the correlation between the magnitude of clockwise hysteresis shown by Ψ and our literature- and observation-based expectations for sediment transport patterns along the river implies that Ψ does actually reflect spatial patterns of bedload transport here, regardless of the specific physical mechanism for this hysteresis.

6.2.3. Alternative sources of hysteresis

Hysteresis in the relationship between seismic shaking and river stage may be produced by several processes in addition to sediment transport. More rain could occur in the first half of a storm, adding rainfall impacts to the seismic signal on the rising limb. A downstream pressure gradient produced by the flood wave on the rising limb, in contrast to the flow-opposing pressure gradient on the falling limb, could produce different flow velocities at a given stage and thereby change the stage-discharge relationship on the rising and falling limbs (Hsu et al., 2011). The stage-discharge relationship or turbulent flow characteristics could also be altered over individual storms due to erosion or deposition.

In both storms, we see no correlation between the rising- and falling-limb discrepancy in seismic amplitude and the same discrepancy in precipitation at any given flow depth, indicating that the increased amplitude on the rising limb is not from rainfall (Supplementary Fig. 10). Further, because the study reach is relatively small (~3 km), both rainfall and pressure-induced changes in flow velocity would have been consistent along the study reach and affected all seismic stations comparably and nearly simultaneously. Therefore, the along-river variation in Ψ during each storm implies that a localized source is responsible for the majority of hysteresis.

Bed evolution (aggradation or erosion such as that addressed in Supplementary Section 4) may have occurred at the radar depth gauge site downstream of the study reach. But as with rainfall and flow velocity, any changes in the stage-discharge relationship at the gauge would have affected all stations equally. Evolution of the local channel form at each seismic station, however, could have contributed to variation in along-river hysteresis effects. The dam reach evolved dramatically over the first storm, and the decrease in slope at the knickpoint (Wang and Kuo, submitted for publication) could have resulted in a decrease in water turbulence on the falling limb.

7. Implications and conclusions

By demonstrating hysteresis at the dam in Storm 1, when transport occurred, and no hysteresis there in Storm 2, when field observations showed a lack of transport, our results directly link the presence of bedload sediment transport to hysteresis in the seismic amplitude observed at a given stage during floods. We develop a numerical metric (Ψ) for the magnitude of hysteresis over individual floods. The exact relationship between Ψ and sediment transport rates has yet to be determined and may vary by location and over time; however, the spatiotemporal patterns in Ψ over the two storms examined here correspond well with bedload transport patterns independently constrained by both field observations and sediment transport gradients inferred from topographic changes. These patterns in Ψ reveal the downstream movement of a sediment pulse over two typhoons following the dam removal. The metric Ψ provides a uniquely focused view of transport patterns over the span of the storms that complements the longer-term transport patterns inferred from topographic changes. The consistent correlation between qualitative patterns in Ψ and sediment transport indicates dominance of transport on the rising limb of each storm, regardless of the relative level of sediment supply on each limb. We therefore speculate that hysteresis at this site arises from time-dependent evolution of the gravel bed, for example due to grain packing, asymmetric fining and coarsening of the bed due to mobile armoring, or the temporal lag between stage and the adjustment of bedforms. The observed transport patterns are consistent with findings from studies (Cui et al., 2003; Sklar et al., 2009; Sutherland et al., 2002; Sutherland et al., 2002) demonstrating both advection and downstream dispersion of sediment pulses.

These results illustrate that hysteresis in the relationship between seismic wave amplitude and river stage may be diagnostic of bedload sediment transport processes in gravel-bed rivers. Analysis of this hysteresis (Ψ) may thus provide a novel means of tracking pulses of bedload sediment liberated during dam removals. Because seismic data can be recorded continuously throughout floods, this approach may offer insight unobtainable through other current monitoring techniques. This application therefore highlights the potential for using continuous, high time resolution seismic data to improve our understanding of rapidly evolving fluvial systems.

Acknowledgements

We thank Victor Tsai and Jim Pizzuto for insightful reviews, and gratefully acknowledge the contributions of Leonard Sklar, Jake Walter, Thorne Lay, Leslie Hsu, Jens Turowski, Ma Kuo-Fong, Ed Boring, Rob Laber, Mikael Witte, Jon Perkins, Chen Yu-Gao, Chen Hong-Yu, He Wan-Yun, Zhang Rui-Ming, Lin Guan-Wei, Zhao Wei-An, Jiang Hong-Wei, Wang Gang-Chuan, Lin Shi-Kai, Jia Hao, Jiao Xuan, and Guo Wei-Cheng. This work was supported by NSF Geomorphology and Land Use Dynamics grant number EAR 1148488. Funding for Open Access provided by the University of California, Santa Cruz, Open Access Fund.

Appendix A. Supplementary material

Supplementary material related to this article can be found online at http://dx.doi.org/10.1016/j.epsl.2014.07.019.

References

Allen, J.R.L., 1974. Reaction, relaxation and lag in natural sedimentary systems: general principles, examples and lessons. Earth-Sci. Rev. 10 (4), 263–342.

Bell, Robert G., Sutherland, Alex J., 1983. Nonequilibrium bedload transport by steady flows. J. Hydraul. Eng. 109 (3), 351–367.

Bogen, J., Møen, K.N.U.T., 2003. Bed load measurements with a new passive ultrasonic sensor. In: Erosion and Sediment Transport Measurement: Technological and Methodological Advances. Oslo, IAHS, pp. 181–192.
Buffington, John M., Montgomery, David R., 1997. A systematic analysis of eight decades of incipient motion studies, with special reference to gravel-bedded rivers. Water Resour. Res. 33 (8), 1993–2029.
Burtin, A., Bollinger, L., Vergne, J., Cattin, Rodolphe, Nábělek, J.L., 2008. Spectral analysis of seismic noise induced by rivers: a new tool to monitor spatiotemporal changes in stream hydrodynamics. J. Geophys. Res., Solid Earth (1978–2012) 113 (B5).
Burtin, A., Vergne, J., Rivera, L., Dubernet, P., 2010. Location of river-induced seismic signal from noise correlation functions. Geophys. J. Int. 182 (3), 1161–1173.
Cantelli, Alessandro, Paola, Chris, Parker, Gary, 2004. Experiments on upstream-migrating erosional narrowing and widening of an incisional channel caused by dam removal. Water Resour. Res. 40 (3).
Charru, François, Mouilleron, H., Eiff, Olivier, 2004. Erosion and deposition of particles on a bed sheared by a viscous flow. J. Fluid Mech. 519, 55–80.
Church, Michael, 2006. Bed material transport and the morphology of alluvial river channels. Annu. Rev. Earth Planet. Sci. 34, 325–354.
Cui, Yantao, Parker, Gary, Lisle, Thomas E., Gott, Julie, Hansler-Ball, Maria E., Pizzuto, James E., Allmendinger, Nicholas E., Reed, Jane M., 2003. Sediment pulses in mountain rivers: 1. Experiments. Water Resour. Res. 39 (9), 1239.
Dietrich, William E., Kirchner, James W., Ikeda, Hiroshi, Iseya, Fujiko, 1989. Sediment supply and the development of the coarse surface layer in gravel-bedded rivers. Nature 340 (6230), 215–217.
Dunne, T., Leopold, L.B., 1978. Water in Environmental Planning. W.H. Freeman, New York.
Emmett, William W., Leopold, Luna B., Myrick, Robert M., 1983. Some characteristics of fluvial processes in rivers. In: US Geological Survey Circular, vol. 953, p. 38.
Exner, F.M., 1920. Zur physik der dünen. Anz. Akad. Wiss. Wien Math.-Nat.wiss. Kl. 129 (2a), 929–952.
Exner, F.M., 1925. Über die wechselwirkung zwischen wasser und geschiebe in flüssen. Anz. Akad. Wiss. Wien Math.-Nat.wiss. Kl. 134 (2a), 165–204.
Griffiths, George A., Sutherland, Alexander J., 1977. Bedload transport by translation waves. J. Hydraul. Div. 103 (11), 1279–1291.
Hsu, Leslie, Finnegan, Noah J., Brodsky, Emily E., 2011. A seismic signature of river bedload transport during storm events. Geophys. Res. Lett. 38 (13).
Humphries, Robert, Venditti, Jeremy G., Sklar, Leonard S., Wooster, John K., 2012. Experimental evidence for the effect of hydrographs on sediment pulse dynamics in gravel-bedded rivers. Water Resour. Res. 48 (1).
Klingeman, P.C., Emmett, W.W., 1982. Gravel bedload transport processes. In: Hey, R.D., Bathurst, J.C., Thornes, C.R. (Eds.), Gravel-Bed Rivers: Fluvial Processes, Engineering and Management. John Wiley, New York, pp. 141–169.
Kuhnle, Roger A., 1992. Bed load transport during rising and falling stages on two small streams. Earth Surf. Process. Landf. 17 (2), 191–197.
Lee, Kwan Tun, Liu, Yi-Liang, Cheng, Kai-Hung, 2004. Experimental investigation of bedload transport processes under unsteady flow conditions. Hydrol. Process. 18 (13), 2439–2454.
Martin, Raleigh L., Jerolmack, Douglas J., 2013. Origin of hysteresis in bed form response to unsteady flows. Water Resour. Res. 49 (3), 1314–1333.
Meyer-Peter, Eugen, Müller, R., 1948. Formulas for bed-load transport. In: Proceedings of the 2nd Meeting of the International Association for Hydraulic Structures Research, pp. 39–64.
Milhous, R.T., Klingeman, P.G., 1992. Bedload transport in mountain streams. In: Specialty Conference. American Society of Civil Engineers, Hydraulics Division. University of Iowa, Iowa City.
Moog, Douglas B., Whiting, Peter J., 1998. Annual hysteresis in bed load rating curves. Water Resour. Res. 34 (9), 2393–2399.
Nanson, Gerald C., 1974. Bedload and suspended-load transport in a small, steep, mountain stream. Am. J. Sci. 274 (5), 471–486.
Parker, Gary, 2005. 1D Sediment Transport Morphodynamics, With Applications to Fluvial and Subaqueous Fans and Fan-Deltas. Ebook.
Reid, Ian, Frostick, Lynne E., Layman, John T., 1985. The incidence and nature of bedload transport during flood flows in coarse-grained alluvial channels. Earth Surf. Process. Landf. 10 (1), 33–44.
Rickenmann, D., McArdell, B.W., 2007. Continuous measurement of sediment transport in the Erlenbach stream using piezoelectric bedload impact sensors. Earth Surf. Process. Landf. 32 (9), 1362–1378.
Schmandt, Brandon, Aster, Richard C., Scherler, Dirk, Tsai, Victor C., Karlstrom, Karl, 2013. Multiple fluvial processes detected by riverside seismic and infrasound monitoring of a controlled flood in the Grand Canyon. Geophys. Res. Lett. 40 (18), 4858–4863.
Sklar, Leonard S., Fadde, Jessica, Venditti, Jeremy G., Nelson, Peter, Wydzga, M. Aleksandra, Cui, Yantao, Dietrich, William E., 2009. Translation and dispersion of sediment pulses in flume experiments simulating gravel augmentation below dams. Water Resour. Res. 45 (8). W08439.
Sutherland, Diane G., Hansler Ball, Maria, Hilton, Susan J., Lisle, Thomas E., 2002. Evolution of a landslide-induced sediment wave in the Navarro River, California. Geol. Soc. Am. Bull. 114 (8), 1036–1048.
Tsai, Victor C., Minchew, Brent, Lamb, Michael P., Ampuero, Jean-Paul, 2012. A physical model for seismic noise generation from sediment transport in rivers. Geophys. Res. Lett. 39 (2).
Turowski, Jens M., Yager, Elowyn M., Badoux, Alexandre, Rickenmann, Dieter, Molnar, Peter, 2009. The impact of exceptional events on erosion, bedload transport and channel stability in a step-pool channel. Earth Surf. Process. Landf. 34 (12), 1661–1673.
Walling, D.E., 1977. Assessing the accuracy of suspended sediment rating curves for a small basin. Water Resour. Res. 13, 531–538.
Wang, H.W., Kuo, W.C., submitted for publication. Geomorphic responses to a large check-dam removal on a mountain river in Taiwan. River Res. Appl.
Whiting, Peter J., Stamm, John F., Moog, Douglas B., Orndorff, Richard L., 1999. Sediment-transporting flows in headwater streams. Geol. Soc. Am. Bull. 111 (3), 450–466.
Wilcock, Peter R., Crowe, Joanna C., 2003. Surface-based transport model for mixed-size sediment. J. Hydraul. Eng. 129 (2), 120–128.
Wohl, Ellen E., Cenderelli, Daniel A., 2000. Sediment deposition and transport patterns following a reservoir sediment release. Water Resour. Res. 36 (1), 319–333.